

Angular momentum transport by internal gravity waves

IV - Wave generation by surface convection zone, from the pre-main sequence to the early-AGB in intermediate mass stars

Suzanne Talon¹ and Corinne Charbonnel^{2,3}

¹ Département de Physique, Université de Montréal, Montréal PQ H3C 3J7, Canada

² Geneva Observatory, University of Geneva, ch. des Maillettes 51, 1290 Sauverny, Switzerland

³ Laboratoire d'Astrophysique de Toulouse et Tarbes, CNRS UMR 5572, OMP, Université Paul Sabatier 3, 14 Av. E.Belin, 31400 Toulouse, France
(talon@astro.umontreal.ca, Corinne.Charbonnel@obs.unige.ch)

Received / Accepted for publication in A&A

ABSTRACT

Context. This is the fourth in a series of papers that deal with angular momentum transport by internal gravity waves in stellar interiors. *Aims.* Here, we want to examine the potential role of waves in other evolutionary phases than the main sequence.

Methods. We study the evolution of a $3 M_{\odot}$ Population I model from the pre-main sequence to the early-AGB phase and examine whether waves can lead to angular momentum redistribution and/or element diffusion at the external convection zone boundary.

Results. We find that, although waves produced by the surface convection zone can be ignored safely for such a star during the main sequence, it is not the case for later evolutionary stages. In particular, angular momentum transport by internal waves could be quite important at the end of the sub-giant branch and during the early-AGB phase. Wave-induced mixing of chemicals is expected during the early-AGB phase.

Key words. Hydrodynamics – Turbulence – Waves – Methods: numerical – Stars: interiors – Stars: rotation

1. Introduction

In recent years, several authors studied the impact of internal gravity waves (IGWs) in a variety of main sequence stars. These waves were initially invoked as a source of mixing in stellar interiors in low-mass stars with an extended surface convection zone (Press 1981; García López & Spruit 1991; Schatzman 1993; Montalbán 1994) and also as an efficient process in the synchronization of massive binary stars (Goldreich & Nicholson 1989). More recently, it was suggested that IGWs may play a role in braking the solar core (Schatzman 1993; Zahn, Talon, & Matias 1997; Kumar & Quataert 1997). This idea was confirmed first in static models (Talon, Kumar, & Zahn 2002) and recently in the complete evolution of solar-mass models, evolved all the way from the pre-main sequence to 4.6 Gy (Charbonnel & Talon 2005).

All these authors find that IGWs are easily excited, and a similar conclusion is reached by studies of convection on top of a stably stratified layer in 2–D and 3–D hydrodynamic numerical simulations (e.g. Hurlburt et al. 1986, 1994; Andersen 1994; Nordlund et al. 1996; Kiraga et al. 2003; Dintrans et al. 2005; Rogers & Glatzmeier 2005a,b). These waves have a strong impact on stellar evolution, especially through their effect on the rotation profile. Through differential filtering, IGWs indeed play a major role in the redistribution of angular momentum in stars, which determines the extent and magnitude of rotation-induced mixing (Talon & Charbonnel 2005, hereafter TC05).

In the spirit of applying a unique set of physical principles to stellar evolution, one needs to assess the impact of such waves

on stars of all masses and at various evolutionary stages. It is our purpose in this series of papers to consistently examine the full Hertzsprung-Russel diagram (HRD) for determining when such waves are efficiently emitted and how they can affect stars when their complete rotational history is being considered.

In Talon & Charbonnel (2003, hereafter Paper I; see also Talon & Charbonnel 1998), we showed how the appearance of IGWs in solar-metallicity main sequence stars with an effective temperature $T_{\text{eff}} \lesssim 6700$ K (i.e., when the surface convection zone becomes substantial) can explain the existence of the lithium dip¹ in stars undergoing rotational mixing.

In Talon & Charbonnel (2004, hereafter Paper II), we examined the IGW generation in Population II main sequence stars. We showed that, along the lithium plateau², the net angular momentum luminosity of IGWs is constant and high enough to enforce quasi solid-body rotation similar to that of the Sun in these stars. We proposed that this behavior could play a major role in explaining the constancy of the lithium abundance in the oldest dwarf stars of our Galaxy (see also a discussion in Charbonnel & Primas 2005).

Here, we wish to look at other evolutionary stages, especially the pre-main sequence (PMS) and the more advanced stages for intermediate-mass stars. We focus in particular on stars in which

¹ The so-called lithium dip, observed in all galactic open clusters older than ≈ 200 Gyr, as well as in the field, refers to a strong lithium depletion in a narrow region of ≈ 300 K in effective temperature, centered around $T_{\text{eff}} = 6700$ K (e.g. Wallerstein et al. 1965; Boesgaard & Tripicco 1986; Balachandran 1995).

² The lithium plateau refers to the constant Li abundance of Population II dwarf stars above $T_{\text{eff}} \approx 5500$ K (e.g. Spite & Spite 1982).

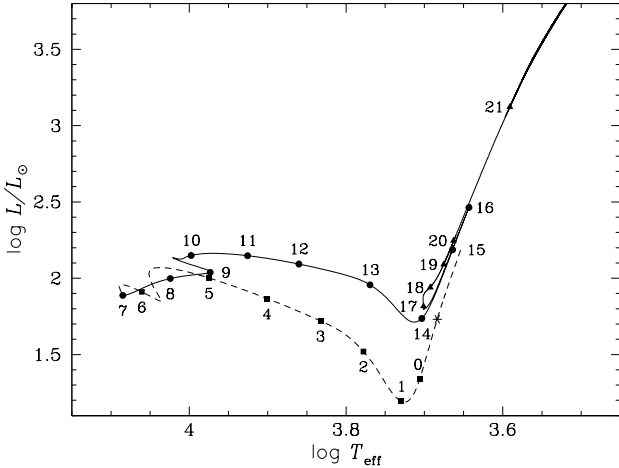


Fig. 1. Evolution of our $3 M_{\odot}$ Pop I model in the HR diagram, from the PMS to the early-AGB. Numbers correspond to selected evolutionary points that are listed in Table 1. For clarity, the PMS is drawn with a dashed line, and the corresponding models are identified by squares, while the star symbol corresponds to the appearance of the convective core. The circles correspond to evolutionary points on the main sequence, sub-giant, and first ascent giant branches, while triangles refer to evolutionary points on the clump and on the early-AGB.

IGWs generation by the surface convection zone is limited on the main sequence, *i.e.*, Pop I star originating from the left side of the Li dip. To do so, we follow the evolution of a $3 M_{\odot}$, $Z = 0.02$ star from the PMS up to the early asymptotic giant branch (early-AGB)³. We estimate at which stages waves are efficiently generated in the outer convection zone. This is a prerequisite for evaluating their impact on the rotation profile of the corresponding stellar models. We also look at the existence of a shear layer oscillation (or SLO) as a direct source of turbulence and mixing at the convective boundary.

We begin in § 2 with a description of the evolution of relevant characteristics for our $3 M_{\odot}$, $Z = 0.02$ star. In § 3, we recall the main aspects of the formalism we used to evaluate the impact of IGWs on stellar evolution. The following sections are devoted to discussing the pre-main sequence (§ 4), the main sequence and the sub-giant branch (§ 5), the red-giant branch (§ 6), and the clump and the early-AGB (§ 7).

2. Evolution of relevant characteristics

In this paper we focus on a $3 M_{\odot}$ with a metallicity $Z = 0.02$ computed with the stellar evolution code STAREVOL (V2.30; Siess et al. 2000). Details regarding the code and the input physics may be found in TC05 and Palacios et al. (2006). The model was computed with classical assumptions, *i.e.*, with neither atomic diffusion nor rotation. Convection is treated using the standard mixing length theory with $\alpha_{\text{MLT}} = 1.75$. The treatment of convection has an impact on the excited wave spectrum (see § 3.1).

When a star evolves, the characteristics that are relevant to wave excitation and to momentum extraction by IGWs change. We thus chose a series of models (*i.e.*, evolutionary points) to correctly represent the evolution of the stellar structure in terms

³ The peculiar case of thermally pulsing AGB (TP-AGB) stars will be presented elsewhere.

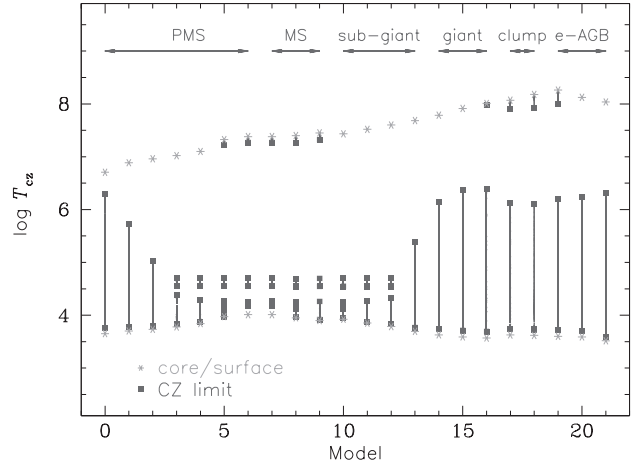


Fig. 2. Evolution of the temperature at the boundaries of convection zones for the evolutionary points selected for the $3 M_{\odot}$ Pop I star and given in Table 1. Core and surface (*i.e.*, T_{eff}) temperatures are also shown. The evolutionary phases are indicated.

of convection zone properties, therefore in terms of IGW characteristics. The position of the selected points along the evolutionary track in the HR diagram for the $3 M_{\odot}$ Pop I star is shown in Fig. 1.

Figure 2 shows the temperature at the boundary of both central and external convection zones at the selected evolutionary points, which is a way to characterize the depth and extension of these regions as the surface and central temperatures (also shown in the figure) of the star evolve. In such an intermediate-mass star, both central hydrogen- and helium-burning occur in a convective core. Wave excitation by core convection on the main sequence is discussed elsewhere (Pantillon et al. 2007, Paper III). Here we only focus on wave excitation by the surface convection zone.

Figures 3 and 4 illustrate the evolution of the main properties that are required to understand the behavior of IGWs in the framework described in § 3. Wave excitation is stronger when the convective scale ℓ_c is larger. However, when the turn-over timescale τ_L becomes too large, this efficiency diminishes. As we shall see in § 3 and subsequent sections, the combination of these two factors produces large differences in the overall efficiency of wave generation as the stellar structure evolves. Another important property for wave-induced transport is the thermal diffusivity K_T at the top of the radiative region. On the main sequence for the star we focus on, K_T is so large that all the low frequency waves (here, we mean waves with $\sigma < 3.5 \mu\text{Hz}$) are dissipated as soon as they are formed, hence the absence of a filtered flux in the corresponding models (see § 5).

Finally, damping also depends strongly on the Brunt-Väisälä frequency (Eq. 7), whose thermal part is given by

$$N_T^2 = \frac{g}{H_p} \delta (\nabla_{\text{ad}} - \nabla) \quad (1)$$

with $\delta = -(\partial \ln \rho / \partial \ln T)_{P,\mu}$, and other symbols have their usual meaning. From Fig. 4 we see that during the PMS, the star's contraction leads to an increase in gravity and a reduction of the pressure scale height, which produce a large increase in N_T^2 when combined. Later, during the giant phase, the expansion of the outer layers produces a large decrease in N_T^2 outside the hydrogen-burning shell. More important, core contrac-

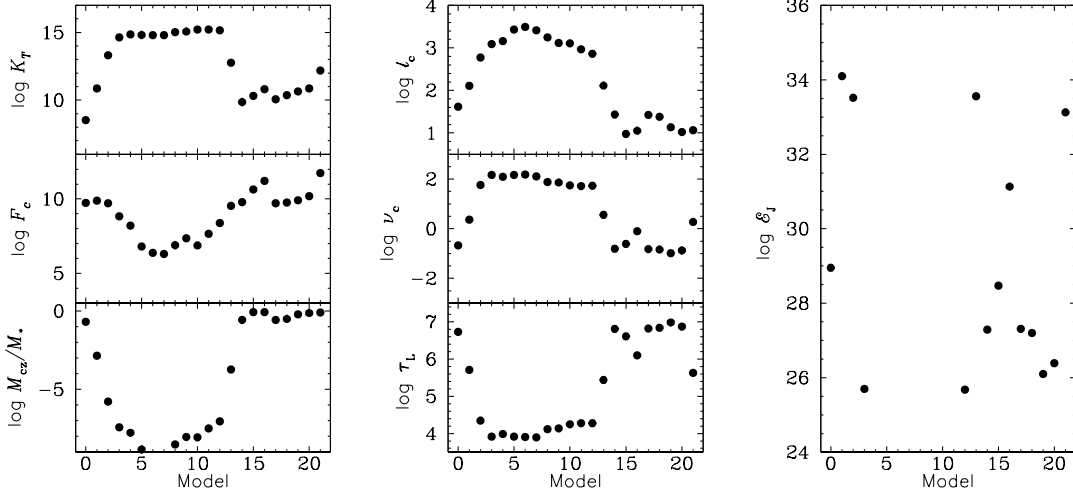


Fig. 3. Evolution of the surface convection zone properties for the $3 M_{\odot}$ Pop I evolutionary points from Table 1. It shows the thermal conductivity K_T (in $\text{cm}^2 \text{s}^{-1}$) at the convective boundary, the convective flux $F_c = \rho v_c^3$ (in g cm^{-3}) taken $0.5 H_P$ into the convection zone, the mass of the convection zone, the spherical harmonic degree corresponding to the convective scale l_c , the convective frequency ν_c (in μHz), the typical convective timescale $\tau_L = \alpha H_P / \nu_c$, as well as the total energy luminosity (in $\text{g cm}^2 \text{s}^{-3}$) prior to any damping in waves (this is for waves with $\nu < 3.5 \mu\text{Hz}$ and $1 < \ell < 60$).

tion produces a major increase inside this shell; in fact, N_T^2 becomes so large there that (low-frequency) waves will be unable to cross that boundary. A large angular momentum deposition is expected there, provided there is differential rotation above to produce a bias in the local wave flux.

3. Formalism

The formalism we use to describe IGW properties is extensively described elsewhere (Papers I and II, and TC05). Here, we only recall the main features of our model and discuss the critical physical principles.

3.1. Wave spectrum

In terms of angular momentum evolution, the relevant parameter is the filtered angular momentum luminosity slightly below the convection envelope (hereafter CE). To get that luminosity, we first need to obtain the spectrum of excited waves. As we did in previous studies, we apply the Goldreich, Murray & Kumar (1994) formalism to IGWs to calculate this spectrum. The energy flux per unit frequency \mathcal{F}_E is then

$$\mathcal{F}_E(\ell, \omega) = \frac{\omega^2}{4\pi} \int dr \frac{\rho^2}{r^2} \left[\left(\frac{\partial \xi_r}{\partial r} \right)^2 + \ell(\ell+1) \left(\frac{\partial \xi_h}{\partial r} \right)^2 \right] \times \exp \left[-h_\omega^2 \ell(\ell+1) / 2r^2 \right] \frac{v_c^3 L^4}{1 + (\omega \tau_L)^{15/2}}, \quad (2)$$

where ξ_r and $[\ell(\ell+1)]^{1/2} \xi_h$ are the radial and horizontal displacement wave functions, which are normalized to unit energy flux just below the convection zone, v_c is the convective velocity, $L = \alpha_{\text{MLT}} H_P$ the radial size of an energy bearing turbulent eddy, $\tau_L \approx L/v_c$ the characteristic convective time, and h_ω is the radial size of the largest eddy at depth r with characteristic fre-

quency of ω or higher ($h_\omega = L \min\{1, (2\omega \tau_L)^{-3/2}\}$). The radial wave number k_r is related to the horizontal wave number k_h by

$$k_r^2 = \left(\frac{N^2}{\sigma^2} - 1 \right) k_h^2 = \left(\frac{N^2}{\sigma^2} - 1 \right) \frac{\ell(\ell+1)}{r^2} \quad (3)$$

where N^2 is the Brunt-Väisälä frequency. In the convection zone, the mode is evanescent and the penetration depth varies as $\sqrt{\ell(\ell+1)}$. The momentum flux per unit frequency \mathcal{F}_J is then related to the kinetic energy flux by

$$\mathcal{F}_J(m, \ell, \omega) = \frac{2m}{\omega} \mathcal{F}_E(\ell, \omega) \quad (4)$$

(Goldreich & Nicholson 1989; Zahn, Talon & Matias 1997). We integrate this quantity horizontally to get an angular momentum luminosity

$$\mathcal{L}_J = 4\pi r^2 \mathcal{F}_J \quad (5)$$

which, in the absence of dissipation, has the advantage of being a conserved quantity (Bretherton 1969; Zahn et al. 1997). This angular momentum luminosity, integrated over $\delta\nu = 0.2 \mu\text{Hz}$, is illustrated in Fig. 5 for our selected evolutionary points, that have low frequency waves with $\nu < 3.5 \mu\text{Hz}$.

Each wave then travels inward and is damped by thermal diffusivity and by viscosity. The local momentum luminosity of waves is given by

$$\mathcal{L}_J(r) = \sum_{\sigma, \ell, m} \mathcal{L}_{J, \ell, m}(r_{cz}) \exp[-\tau(r, \sigma, \ell)] \quad (6)$$

where ‘cz’ refers to the base of the convection zone. τ corresponds to the integration of the local damping rate and takes into account the mean molecular weight stratification

$$\tau(r, \sigma, \ell) = [\ell(\ell+1)]^{3/2} \int_r^{r_c} (K_T + \nu_v) \frac{NN_T^2}{\sigma^4} \left(\frac{N^2}{N^2 - \sigma^2} \right)^{1/2} \frac{dr}{r^3} \quad (7)$$

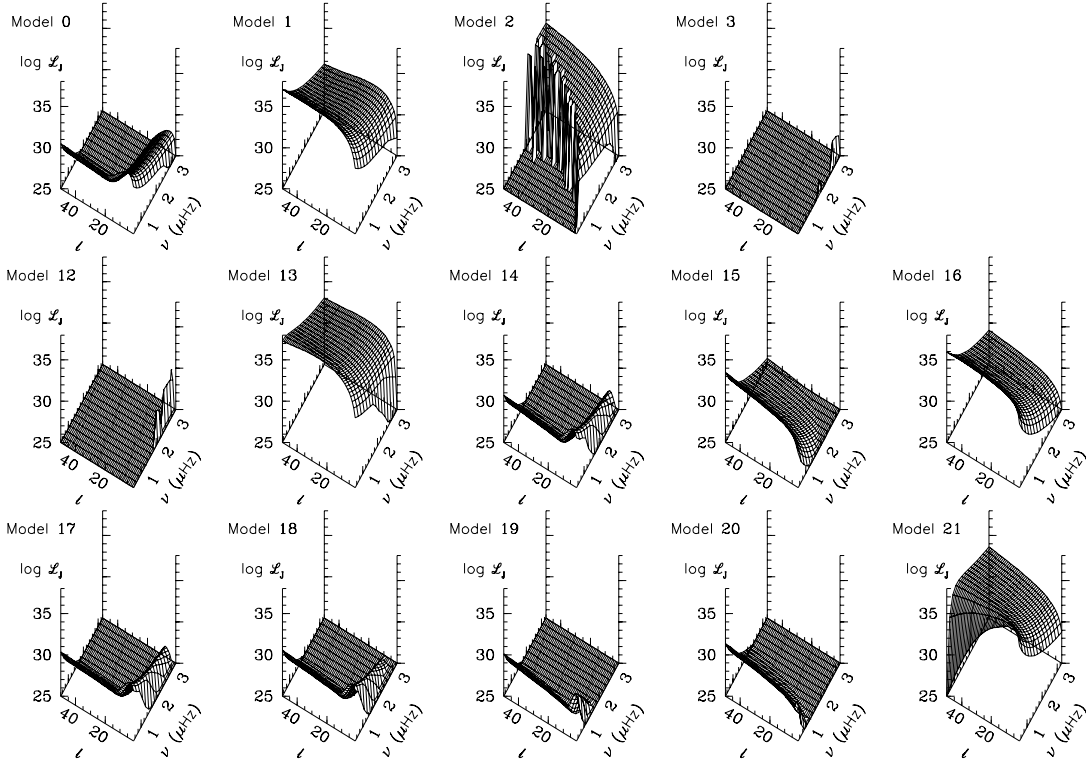


Fig. 5. Evolution of the spectrum of angular momentum luminosity integrated over $\delta\nu = 0.2 \mu\text{Hz}$ (in g s^{-3} prior to any damping of IGWs on the PMS (upper row) and from the giant branch to the early AGB in the $3 M_{\odot}$ Pop I star. Models 4 to 11 have no waves with $\nu < 3.5 \mu\text{Hz}$ and are thus not shown here.

(Zahn et al. 1997). In this expression, N_T^2 is the thermal part of the Brunt-Väisälä frequency (see Eq. 1), K_T the thermal diffusivity, and ν_v the (vertical) turbulent viscosity. Finally σ is the local, Doppler-shifted frequency

$$\sigma(r) = \omega - m [\Omega(r) - \Omega_{\text{cz}}] \quad (8)$$

and ω is the wave frequency in the reference frame of the convection zone. Let us mention that only the radial velocity gradients are taken into account in this expression for damping. This is because angular momentum transport is dominated by the low-frequency waves ($\sigma \ll N$), which implies that horizontal gradients are much smaller than vertical ones (cf. Eq. 3).

When meridional circulation, turbulence, and waves are all taken into account, the evolution of angular momentum follows

$$\rho \frac{d}{dt} [r^2 \Omega] = \frac{1}{5r^2} \frac{\partial}{\partial r} [\rho r^4 \Omega U] + \frac{1}{r^2} \frac{\partial}{\partial r} \left[\rho \nu_v r^4 \frac{\partial \Omega}{\partial r} \right] - \frac{3}{8\pi} \frac{1}{r^2} \frac{\partial}{\partial r} \mathcal{L}_J(r) \quad (9)$$

(Talon & Zahn 1998), where U is the radial meridional circulation velocity. Horizontal averaging was performed for this equation, and meridional circulation was considered only at first order. In this paper, this equation is used only to calculate the fast SLO's dynamics (see § 3.2) and thus, U is neglected. The complete equation is used when longer timescales are involved as discussed *e.g.* in Charbonnel & Talon (2005).

In this work, we neglect any contribution from convective overshoot due to the lack of a usable prescription (although work

is underway to include this effect, Belkacem et al., in preparation). We expect this contribution to be more efficient for low-frequency, low-degree waves, and as such, it would have an impact mostly on the timescale for angular momentum extraction in the core (see § 3.3).

3.2. Shear layer oscillation (SLO)

One key feature when looking at the wave-mean flow interaction is that the dissipation of IGWs produces an increase in the local differential rotation, which is caused by the increased dissipation of waves that travel in the direction of the shear (see Eqs. 7 and 8). In conjunction with viscosity, this leads to the formation of an oscillating doubled-peak shear layer that oscillates on a short timescale (Gough & McIntyre 1998; Ringot 1998; Kumar, Talon & Zahn 1999). This shear layer oscillation (hereafter SLO) occurs if the deposition of angular momentum by IGWs is large enough when compared with viscosity⁴ (Kim & MacGregor 2001; see also a discussion in TC05, § 3.1.).

To calculate the turbulence associated with this oscillation, we relied on a standard prescription for shear turbulence away from regions with mean molecular weight gradients

$$\nu_v = \frac{8}{5} Ri_{\text{crit}} K_T \frac{(rd\Omega/dr)^2}{N_T^2}, \quad (10)$$

⁴ When the wave flux is too small, one simply reaches a stationary regime where the angular momentum deposition by IGWs is compensated by viscous diffusivity.

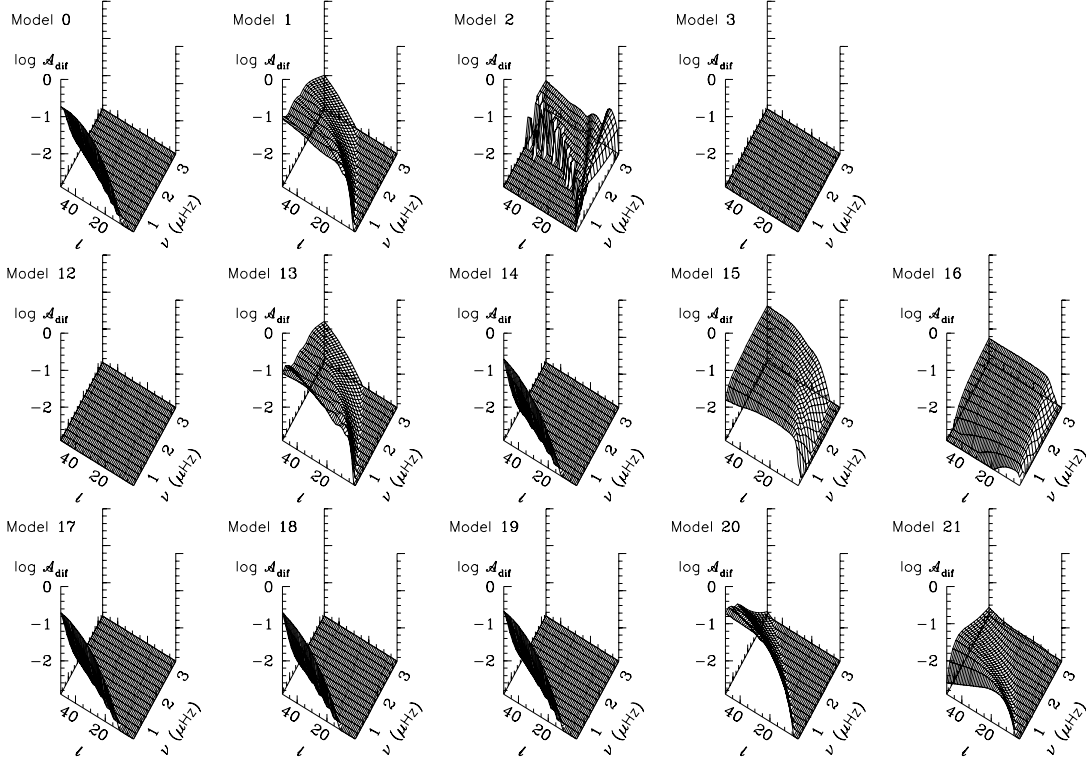


Fig. 6. Differential wave amplitude variation over a depth of $0.05 R_*$ (see text).

which takes radiative losses into account (Townsend 1958; Maeder 1995). This coefficient is time-averaged over a complete oscillation cycle (for details, see TC05, § 3.1).

The first feature we are interested in is whether or not the formation of such an SLO is possible at various evolutionary stages, since the associated turbulence could produce mixing in a small region below the surface convection zone. Figure 6 shows the differential wave amplitude variation in the region of SLO formation. The plotted quantity corresponds to

$$\mathcal{A}_{\text{dif}} = \sum_{r_{\text{cz}}}^{r_{\text{cz}}+0.05 R_*} |\Delta A_{\text{prograde}} - \Delta A_{\text{retrograde}}| \quad (11)$$

where ΔA corresponds to the local amplitude variation, caused by radiative damping (see Eq. 7) for the $\ell = m$ wave and for a local gradient of $0.001 \mu\text{Hz}/0.05 R_*$. This choice of differential rotation is quite arbitrary, but TC05 (see their § 3.2) show that, as long as differential rotation is not too strong (that is, it remains below about $1 \mu\text{Hz}/0.05 R_*$), differential damping is linear. The value of $0.05 R_*$ is typical of the thickness of the SLO (TC05). When \mathcal{A}_{dif} is large, prograde and retrograde waves are deposited at different locations in the region of SLO formation and thus contribute to the potential generation of an SLO. As the wave frequency rises, the Doppler shift is felt less by the star and \mathcal{A}_{dif} remains small. For frequencies that are too low, the waves can be damped even before the Doppler shift may take place (see e.g. Model 1).

To discuss the formation of the SLO, \mathcal{A}_{dif} should be multiplied by the angular momentum luminosity of waves, which is shown in Fig. 5 for the GMK model. This was done for example for models 13 and 15 in Fig. 7. For these two models, the waves that would give rise to the appearance of an SLO are quite similar, as the differential amplitude figure shows (Fig. 6). However,

there is an SLO only in model 13, because in model 15, the wave angular momentum luminosity corresponding to such waves is simply too small. We note that, for any other excitation model, an SLO would be obtained for an angular momentum luminosity on the order of $10^{33} - 10^{34}$ (or more) in the region with $\mathcal{A}_{\text{dif}} \approx 0.01$ to 0.1. Therefore, for any excitation model we can rapidly evaluate whether an SLO should develop from our Fig. 6.

The existence of such an SLO has been challenged by Rogers & Glatzmeier (2006, hereafter RG06). In 2-D numerical simulations of penetrative convection in the Sun, they find that IGWs are efficiently excited by convection, as did the other authors who studied this (Hurlburt et al. 1986, 1994; Andersen 1994; Nordlund et al. 1996; Kiraga et al. 2003; Dintrans et al. 2005; Rogers & Glatzmeier 2005a,b). In these simulations, wave spectra are much broader than the ones predicted in theoretical models based on Reynolds stresses (Kumar, Talon, & Zahn 1999, hereafter KTZ99). However, contrary to the expectations of other authors (see in particular the discussion by Kiraga et al. 2003), RG06 obtain an energy flux⁵ that is smaller *in the low-frequency regime* than the one calculated by KTZ99, and that, even though one expects the excitation by convective plumes that has been ignored by KTZ99 to yield a large contribution to wave generation.

⁵ In their simulation, which has a lower Reynolds number than the Sun, but a larger convective flux, the total wave flux is rather large, and it scales as

$$F_{\text{waves}} = F_T \frac{v}{c_s} \quad (12)$$

with F_T the total flux, v the velocity of turbulent eddies and c_s the sound velocity.

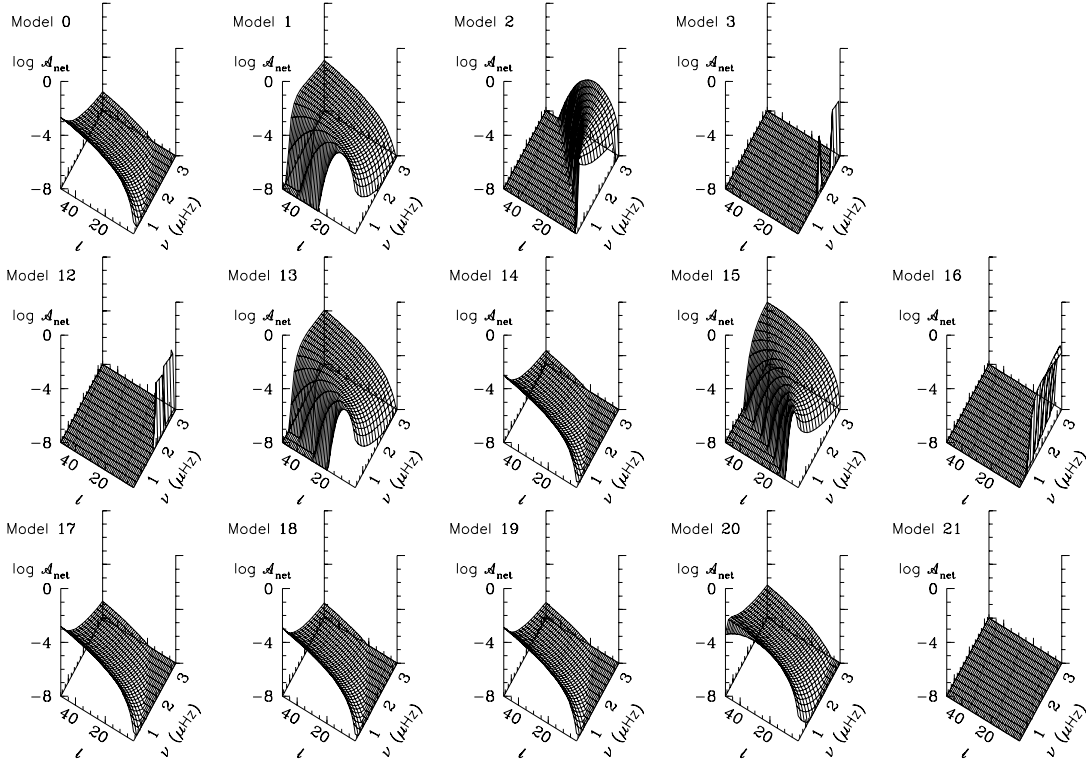


Fig. 8. Net wave amplitude beyond a depth of $0.05 R_*$ (see text).

In their simulations, RG06 thus have a much weaker wave flux in the low-frequency regime than what is required to generate an SLO (see the above discussion on Fig. 7), although the one for the high frequency waves is much larger. It may thus not be surprising that RG06 do not find such an SLO in their simulation. Furthermore, the size of the SLO being smaller (in KTZ99) than the difference between the rotation rate at the base of the convection zone (at the equator) and the base of the tachocline, an SLO would not appear as a shear reversal in their simulation. Last, the RG06 simulation is simply not long enough to show the SLO. As pointed out by the authors, in their numerical simulation there is differential rotation in the tachocline driven by convective plumes. But the total duration of the simulation being only one year, it would be impossible to see a superposed SLO since its timescale is expected to be of about a few years, according to the KTZ99 calculations. Furthermore, since RG06 have a reduced wave flux compared to KTZ99, this timescale would be even longer, and thus clearly beyond the possibilities of the RG06 simulation.

3.3. Filtered angular momentum luminosity

We must also look at the secular effect of IGWs in the deep interior (see TC05 for details). In the presence of differential rotation, the dissipation of prograde and retrograde waves in the SLO is not symmetric, and this leads to a finite amount of angular momentum being deposited in the interior beyond the SLO. Figure 8 shows the net amplitude of waves at a depth of $0.05 R_*$, defined by

$$\mathcal{A}_{\text{net}} = A_{\text{retrograde}} - A_{\text{prograde}} \quad (13)$$

for a local gradient of $0.001 \mu\text{Hz}/0.05 R_*$. Multiplied by the angular momentum luminosity of waves, this is the filtered angular momentum luminosity $\mathcal{L}_J^{\text{fil}}$ given in Table 1 for our selected evolutionary points. Let us mention that, in fact, the existence of an SLO is not even required to obtain this differential damping between prograde and retrograde waves, so as long as differential rotation exists at the base of the convection zone, waves will have a net impact on the rotation rate of the interior. The timescale required to delete the imposed differential rotation is of the order of

$$\tau = I \delta \Omega / \mathcal{L}_J^{\text{fil}}. \quad (14)$$

The SLO's dynamics is studied by solving Eq. (9) with small timesteps and using the whole wave spectrum, while for the secular evolution of the star, one has to instead use the filtered angular momentum luminosity (see TC05 for details). All the relevant quantities are given in Table 1 for our selected evolutionary points. Let us also mention here that differential damping is required both for the SLO and for the filtered angular momentum luminosity. Since this relies on the Doppler shift of the frequency (see Eqs. 7 and 8), angular momentum redistribution will be dominated by the low-frequency waves, which experience a larger Doppler shift, but that is not so low that they will be immediately damped. Numerical tests indicate that this occurs around ($\sigma \approx 1 \mu\text{Hz}$).

4. Pre-main sequence

We start with a fully convective contracting star. As it descends along the Hayashi track, a radiative core appears (Fig. 1). In mass coordinates, the top of this radiative region migrates towards the

Table 1. Selected models along the evolutionary track of a $3 M_{\odot}$ Pop I star. The filtered angular momentum luminosity $\mathcal{L}_J^{\text{fil}}$ is taken as $0.05 R$ below the CZ (or at $R_{\text{cz}}/2$ if it is larger) for a differential rotation of $\delta\Omega = 0.001 \mu\text{Hz}$. Also provided are the star's moment of inertia of the radiative zone I_R and the resulting timescale $\tau = I_R \delta\Omega / \mathcal{L}_J^{\text{fil}}$ for IGWs. The last column gives the time Δt between consecutive models (with the convention $\Delta t_i = t_{i+1} - t_i$). No waves are generated in models 4 to 11.

Model	Evolutionary Status	SLO	$\mathcal{L}_J^{\text{fil}}$ ($\text{g cm}^2 \text{s}^{-2}$)	I_R (g cm^2)	τ (yr)	Δt (yr)
0	PMS	no	-3.4×10^{32}	7.7×10^{55}	4.5×10^7	7.2×10^5
1		yes	-2.5×10^{37}	7.4×10^{55}	5.8×10^3	7.7×10^5
2		yes	-1.5×10^{35}	5.5×10^{55}	7.1×10^4	3.1×10^5
3		no	-9.2×10^{24}	4.2×10^{55}	9.2×10^{14}	2.0×10^5
4		no	–	–	–	2.0×10^5
5		no	–	–	–	8.8×10^5
6	no	–	–	–	8.8×10^6	
7	MS	no	–	–	–	2.2×10^8
8		no	–	–	–	7.9×10^7
9		no	–	–	–	1.3×10^7
10	sub-giant	no	–	–	–	7.9×10^6
11		no	–	–	–	1.4×10^6
12		no	-9.5×10^{26}	5.2×10^{55}	1.1×10^{13}	9.6×10^5
13		yes	-5.5×10^{36}	1.0×10^{56}	3.8×10^3	9.8×10^5
14	giant	no	-1.9×10^{31}	1.6×10^{56}	1.7×10^9	1.9×10^6
15		no	-4.9×10^{27}	1.4×10^{54}	5.6×10^{10}	1.5×10^6
16		yes	-1.6×10^{28}	1.8×10^{53}	2.2×10^9	4.6×10^7
17	clump	no	-8.0×10^{30}	1.8×10^{56}	4.4×10^9	9.4×10^7
18		no	-1.3×10^{31}	1.9×10^{56}	2.9×10^9	9.8×10^6
19	early AGB	no	-4.7×10^{30}	5.9×10^{55}	2.5×10^9	1.1×10^7
20		no	-2.7×10^{30}	1.2×10^{55}	9.0×10^8	8.0×10^6
21		yes	-1.0×10^{29}	2.4×10^{52}	4.7×10^7	

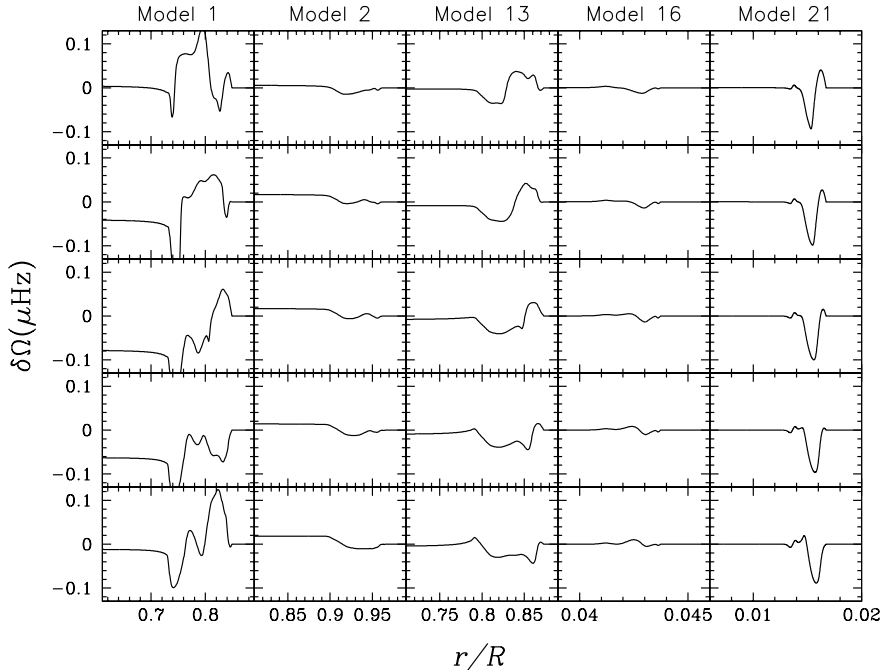


Fig. 9. Shear layer oscillation in the $3 M_{\odot}$ Pop I model at the evolutionary points where this feature appears. For each evolutionary point, successive profiles are separated by $\Delta t = 5$ yr.

surface until the star reaches the main sequence. This is accompanied by a growth of the characteristic convective length scale at the bottom of the convection zone $\ell_c = 2\pi r_{\text{cz}}/\alpha H_P$ (see Fig. 3), which temporarily favors the generation of waves (see models 0 to 2).

However, with further retraction of the envelope, the thermal diffusivity K_T at the convective boundary increases, which favors the disappearance of low-frequency and/or large degree waves (see Fig. 5 and Eq. 7). This explains the reduction of the total energy flux at the end of the PMS (models 3 to 6) and on the MS.

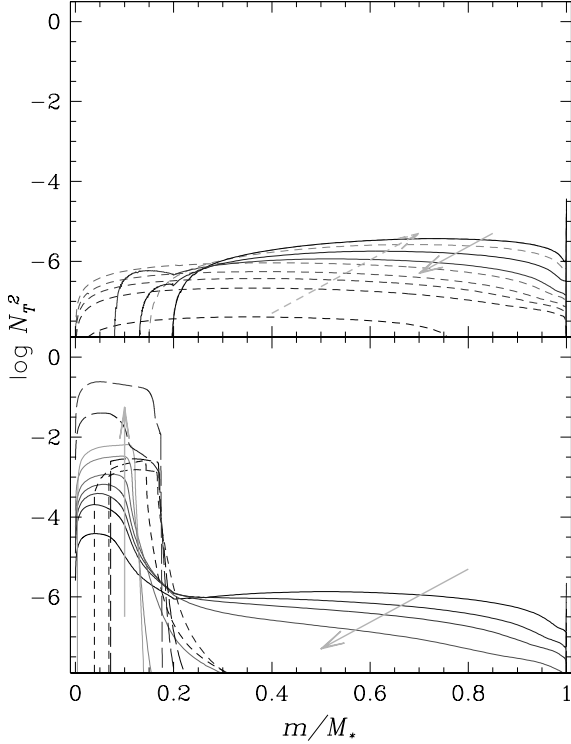


Fig. 4. Evolution of the (thermal part of the) Brunt-Väisälä frequency vs mass for our $3 M_{\odot}$ Pop I star. (Top) The dashed lines correspond to PMS models and the continuous lines, to MS models. In PMS models, N_T^2 increases with evolution, while it decreases in MS models. The shade of gray becomes lighter for more evolved models. The dashed arrow corresponds to the evolution during the PMS and the continuous one to the evolution during the MS. (Bottom) The continuous lines correspond to sub-giants and giants, the short-dashed lines to the clump, and the long-dashed lines to early-AGB models. In the outer layers, N_T^2 diminishes with time while it is the opposite in the core. The arrows indicate time evolution.

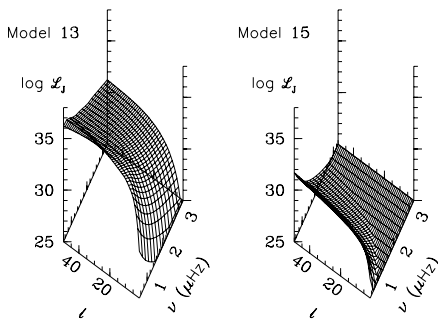


Fig. 7. Differential wave angular momentum luminosity variation over a depth of $0.05 R_*$ for models 13 and 15.

During the pre-main sequence, an SLO exists only for a very short period of time. The evolution of the SLO for models 1 and 2 is shown in Fig. 9, where the successive profiles are separated by 5 years. The larger amplitude in model 1 compared to model 2 can be understood in terms of thermal diffusivity: since K_T increases with radius, as the top of the radiative zone

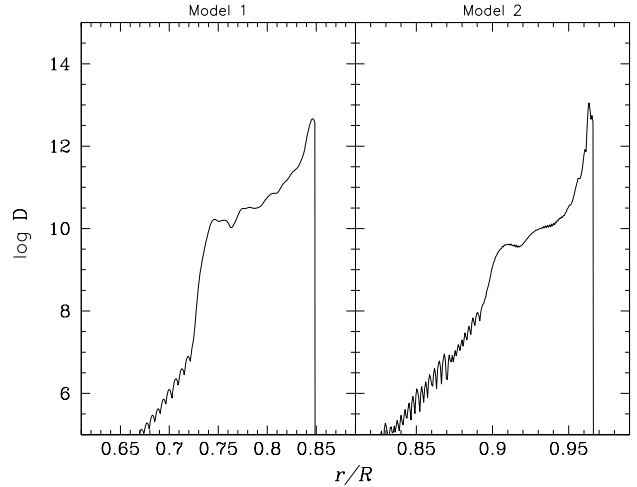


Fig. 10. Turbulent wave-induced diffusion coefficient at the convection zone boundary on the pre-main sequence in the $3 M_{\odot}$ Pop I star

migrates outwards with evolution, waves are dissipated more efficiently in model 2 than in model 1. In model 3, damping is so large that the formation of a SLO is no longer possible, and all low-frequency waves are dissipated in model 4. The turbulent diffusion coefficient associated with this SLO, D (see Eq. 10 and the discussion around it), is shown in Fig. 10 as a function of reduced radius. While the shear is much stronger in model 1 than in model 2, the magnitude of D and width of the turbulent regions are quite similar. This is because the reduced shear is compensated for by the larger thermal diffusivity in model 2 (*cf.* Eq. 10). In both models, D is relatively high just below the convective envelope, and it drops rapidly with depth. It is negligible in the region with a temperature (*i.e.* $T \gtrsim 2.5 \times 10^6$ K) high enough for efficient lithium burning. This temperature is attained at reduced radii of $r/R \sim 0.43$ and 0.41 in models 1 and 2 respectively. This implies that, for this mass, the transport of elements through wave-induced turbulence has no impact on the pre-main sequence evolution of the surface abundance of the light elements such as lithium, beryllium, or boron (the latest two elements burning at an even higher temperature)⁶.

The role of IGWs is more uncertain for the rotation profile. In the case of rapid rotation ($v \gtrsim 100 \text{ km s}^{-1}$), the initial rotation profile is deleted by meridional circulation in a fraction of the main-sequence lifetime. In a slow rotator, however, this is not the case, and the memory of angular momentum transport by IGWs will influence mixing⁷. Detailed evolutionary calculations of angular momentum in the presence of internal waves should thus take this evolutionary phase into account especially in the case of slow rotators (Charbonnel & Talon, in preparation).

5. Main sequence and sub-giant branch

On the main sequence (models 7 to 9) and early on the sub-giant branch (models 10 and 11), the surface convection zone of the star remains quite shallow and contains no more than $\sim 3 \times 10^{-8} M_*$. In the bottom part of the convection zone, which is the

⁶ No LiBeB depletion is expected on the PMS in a classical model for a Pop I star of that mass, that is due to the CE base too cool during that phase (see Fig. 2).

⁷ The role of the evolution of the rotation profile on main sequence mixing is discussed further in Talon, Richard & Michaud (2006), § 3.2.

main driver of IGWs, the mean convective flux is too small ($\sim 0.001 L_\odot$) to excite IGWs efficiently (see Fig. 3). Furthermore, the thermal diffusivity below the convection zone is quite large, and perturbations traveling into the radiative zone are rapidly damped instead of becoming waves. This is the case in particular for all the low-frequency waves that are needed for driving an SLO⁸ (for waves with a frequency $\nu < 3.5 \mu\text{Hz}$, $\mathcal{F}_J = 0$). There is thus no SLO or any secular effect on the rotation profile from this exterior convection zone, both on the MS and at the beginning of the sub-giant branch in such an intermediate-mass star.

This result agrees with the conclusions of Paper I, i.e., the total momentum luminosity in waves drops dramatically in main sequence Pop I stars with initial masses higher than $\sim 1.4 M_\odot$, i.e. stars originating from the left side of the Li dip, compared to stars with lower initial mass.

Angular momentum transport by IGWs becomes important as the star moves farther along the sub-giant branch. Indeed the retraction of the convective envelope is accompanied by a diminution of the thermal diffusivity and an increase in the convective flux. To properly assess the importance of waves in the star's rotation, we should compare the timescale τ (Eq. 14) with the lifetime of various evolutionary stages; both quantities are given in Table 1. Model 13 is of special interest here because it lies at the end of the sub-giant branch (see Fig. 1) and supports a particularly large wave flux, due to a unique combination of many factors (including the convective time- and length-scales, see Fig. 3). This implies that possible differential rotation, which could be a relic of the star's main sequence history and subsequent contraction, will be strongly reduced by IGWs when the star leaves the Hertzsprung gap. This will have a profound impact on the subsequent evolution. Let us also mention that, close to the core, waves could actually create a large differential rotation. This was observed in the numerical simulation by RG06 and is also visible when one looks at the Fig. 3 of Talon et al. (2002), where, close to the core, strong shears appear in the early stages of the simulation. Detailed calculations, including meridional circulation, shear turbulence, and wave induced angular momentum transport, are required to come to any conclusion other than that the wave will have a strong impact at this stage.

6. Red giant branch

As the star evolves to the red giant branch, the surface convection zone deepens, and the thermal conductivity below the convection envelope is reduced with the photon mean free path (models 12 to 16, see Fig. 3). Wave excitation during this phase is quite similar to what has been observed in PMS stars.

A SLO appears at the tip of the RGB (Model 16). The corresponding diffusion coefficient is shown in Fig. 11, together with the abundance profile of the lightest elements that are affected by shell hydrogen-burning. These quantities are plotted against δM , which is a relative mass coordinate allowing for a blow-up of the radiative region above the hydrogen-burning shell (hereafter HBS) and is defined as

$$\delta M = \frac{M_r - M_{\text{HBS}}}{M_{\text{BCE}} - M_{\text{HBS}}}. \quad (15)$$

Here δM is equal to 1 at the base of the convective envelope and 0 at the base of the HBS (where $X = 10^{-7}$). The abundance profiles at that phase have been modified by dilution during the first dredge-up episode and are being reconstructed by shell

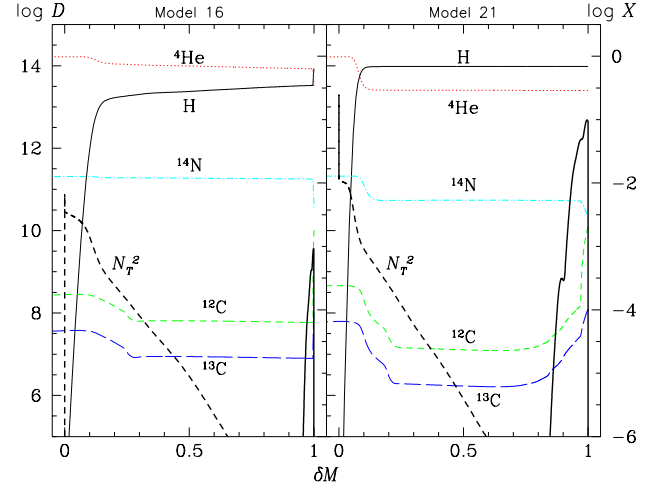


Fig. 11. Turbulent wave-induced diffusion coefficient at the convection zone boundary in the $3 M_\odot$ Pop I star (left) on the red giant branch and (right) on the early-AGB (wide continuous curve, left scale). Superimposed is the logarithm of the mass fraction of H, ^4He , ^{12}C , ^{13}C and ^{14}N (right scale). The abscissa is the scaled mass coordinate δM which equals 0 at the base of the hydrogen-burning shell and 1 at the base of the CE (see text). Also shown is the Brunt-Väisälä frequency (wide dashed curve, right scale).

hydrogen-burning. We see that D drops very rapidly just below the CE. Additionally, the star leaves that phase very rapidly. As a consequence, wave-induced turbulence is not expected to modify the surface abundances on the RGB for such an intermediate-mass Pop I star.

The rotation profile should hardly be influenced by IGWs for that star on the RGB, in view of the timescale τ (Eq. 14) which is now almost two orders of magnitude higher than the lifetime at that stage (see Table 1).

7. Clump and early-AGB

Model 16 marks the ignition of central He-burning in the non-degenerate core, and model 17 corresponds to the arrival of the star in the so-called clump in the HR diagram. At that moment the convective envelope strongly retreats in mass, before deepening again slowly until the central exhaustion of helium, which occurs for model 18⁹. Then the star moves to the early-AGB. During that period, the total energy flux in waves remains relatively modest and there is no SLO.

The situation changes drastically in model 21 however. At that point, the convective envelope has reached its maximum depth, which stays almost constant until the first thermal pulse occurs (at $\Delta t \approx 4 \times 10^5$ yr after model 21). During that second dredge-up, the convective envelope has engulfed most (but not all) of the more external step of the ^{14}N profile left behind by the CN-cycle, which explains the steep gradients in the abundance profiles of that element and of the carbon isotopes just below the convective envelope. In this region, D is relatively high, and we expect that the associated mixing leads to an additional slight variation in the surface abundance of ^{12}C and ^{13}C (but not of the

⁹ The variations in the depth of the CE at that phase are hardly seen in Fig. 3, because the total variations represented for $\log(M_{\text{cz}}/M_*)$ cover nine orders of magnitude. However, the value for $\log(M_{\text{cz}}/M_*)$ in models 16, 17, and 21 is -0.854, -0.138, and -0.747, respectively.

⁸ We recall that thermal damping is proportional to $1/\sigma^4$, see Eq. 7.

carbon isotopic ratio since CN is at the equilibrium), and of ^{14}N with respect to standard second dredge-up.

For the transport of angular momentum, the rapid increase in the Brunt-Väisälä frequency in the HBS could produce strong shears that, in complete calculations taking rotational mixing into account, would be an important source of mixing during the early-AGB. This would modify the composition close to the core and would strongly modify the subsequent evolution.

8. Conclusion

In this paper, we examined when and how internal gravity waves generated by surface convection zones are expected to have an impact on stellar models that only have shallow surface convection zones during the main sequence. We find that several evolutionary stages can experience angular momentum redistribution by IGWs:

- During the pre-main sequence, just as the star leaves the Hayashi track, waves are efficiently excited and filtered. While this has no impact on light element abundances and only has a limited effect on fast rotators (see § 4), it could strongly modify the main-sequence rotation profile of slow rotators;
- At the end of the sub-giant branch (*i.e.*, at the boundary of the Hayashi track), angular momentum redistribution is once more quite efficient and could totally change the angular momentum profile that has been established during the main sequence and the sub-giant phase contraction;
- During the early-AGB, IGW generation again becomes substantial: mixing can be expected to occur both at the convective boundary, due to the presence of an SLO and at the hydrogen-burning-shell boundary, due to the enhanced damping of waves caused by the increase in the Brunt-Väisälä frequency.

Stellar models including meridional circulation, shear turbulence, and wave-induced mixing are underway to quantify this impact (Charbonnel & Talon, in preparation).

Acknowledgements. We thank the referee for her/his comments that helped us improve the manuscript. CC is supported by the Swiss National Science Foundation (FNS). We acknowledge the financial support of the Programme National de Physique Stellaire (PNPS) of CNRS/INSU, France. Computational resources were provided by the Réseau québécois de calcul de haute performance (RQCHP).

References

Andersen B.N., 1994, *Solar Phys.* 152, 241
 Balachandran S., 1995, *ApJ*, 446, 203
 Boesgaard, A.M., Tripicco, M.J., 1986, *ApJ*, 302, L49
 Bretherton F.P., 1969, *Quart. J. R. Met. Soc.* 95, 213
 Charbonnel, C., Primas, F., 2005, *A&A*, 442, 961
 Charbonnel, C., Talon, S., 2005, *Science*, 309, 2189
 Dintrans B., Brandenburg A., Nordlund Å, Stein R.F., 2005, *A&A* 438, 365
 García López R.J., Spruit H.C., 1991, *ApJ* 377, 268
 Goldreich P., Murray N., Kumar, P., 1994, *ApJ* 424, 466
 Goldreich P., Nicholson P.D., 1989, *ApJ* 342, 1079
 Gough D.O., McIntyre M.E., 1998, *Nature* 394, 755
 Kim Eun-jin, MacGregor K.B., 2001, *ApJ* 556, L117
 Kiraga M., Jahn K., Stepień K., Zahn J.-P., 2003, *Acta Astronomica*, 53, 321
 Kumar P., Quataert E.J., 1997, *ApJ* 475, L143
 Kumar P., Talon S., Zahn J.-P., 1999, *ApJ* 520, 859
 Hurlburt N.E., Toomre J., Massaguer J.M., 1986, *ApJ* 311, 563
 Hurlburt N.E., Toomre J., Massaguer J.M., Zahn J.-P., 1994, *ApJ* 421, 245
 Maeder A., 1995, *A&A* 299, 84
 Montalbán J., 1994, *A&A* 281, 421

Nordlund A., Stein R.F., Brandenburg A., 1996, *Bull. Astron. Soc. of India* 24, 261
 Palacios A., Charbonnel C., Talon S., Siess L., 2006, *A&A* 453, 261
 Pantillon F.P., Talon S., Charbonnel C., 2007, *A&A*, 474, 155 (Paper III)
 Press W.H., 1981, *ApJ* 245, 286
 Ringot O., 1998, *A&A* 335, 89
 Rogers T.M., Glatzmeier G.A., 2005a, *ApJ* 620, 432
 Rogers T.M., Glatzmeier G.A., 2005b, *MNRAS* 364, 1135
 Rogers T.M., Glatzmeier G.A., 2006, *ApJ*, 653, 765 (RG06)
 Schatzman E., 1993, *A&A* 279, 431
 Siess L., Dufour E., & Forestini M. 2000, *A&A* 358, 593
 Spite, M., Spite, F., 1982, *Nature* 297, 483
 Talon S., Charbonnel C., 1998, *A&A* 335, 959
 Talon S., Charbonnel C., 2003, *A&A* 405, 1025 (Paper I)
 Talon S., Charbonnel C., 2004, *A&A* 418, 1051 (Paper II)
 Talon S., Charbonnel C., 2005, *A&A* 440, 981, TC05
 Talon S., Kumar P., Zahn J.-P., 2002, *ApJL* 574, 175
 Talon S., Richard, O., Michaud, G., 2006, *ApJ*, 645, 634
 Talon S., Zahn J.-P., 1998, *A&A* 329, 315
 Townsend A.A., 1958, *J. Fluid Mech.* 4, 361
 Wallerstein, G., Herbig, G.H., Conti, P.S., 1965, *ApJ* 141, 610
 Zahn J.-P., Talon S., Matias J., 1997, *A&A* 322, 320